THE RELATIONSHIP BETWEEN LAND USE/LAND COVER AND AEROSOL OPTICAL DEPTH VARIATION IN HANOI CITY

Danh Tuyen Vu[1,*], Anh Huy Hoang[1], Tien Thanh Nguyen[1]

[1]*Hanoi University of Natural Resources and Environment*

DOI: 10.56651/lqdtu.jst.v6.n01.666.sce

Abstract

This study investigates the relationship between AOD variation and different land use/land cover (LULC) types. These LULC types were first classified from Landsat 9 images using the maximum likelihood classification (MLC) method. The AOD variation for each LULC type acquired from MODIS imagery was then extracted using the mask method. The statistical parameters for the AOD variation in each LULC were summarized and compared. It was found that there existed a close relationship (a positive correlation) between the AOD variation and water bodies and built-up land. Lower AOD values were usually distributed in greening land and crop land whereas the lowest AOD values were mainly concentrated in forest and river sand.

Keywords: *Relationship; land use and land cover; AOD; Landsat 9 and MODIS images.*

1. Introduction

The aerosol optical depth (AOD) is a key aerosol property, and is the main physical quantity characterizing the atmospheric turbidity [1, 2]. Aerosol is also an important constituent of the atmosphere, and plays a key role in the radiation balance, regional and global climate change, and human health [3, 4]. Aerosol is released to the atmosphere through both natural and anthropogenic processes [5]. AOD represents extinction of light over the vertical column of the atmosphere. As an important measure of aerosol loading, AOD is a crucial metric in assessment of global climate change and the impact of aerosol on precipitation, radiation, and clouds [6]. Understanding of driving factors and its impacts on AOD variation plays an important role in the improvement of air quality.

Due to rapid industrial development, air pollution has become a serious problem in the regions where people live [5]. Therefore, to have a better understanding of aerosol, a lot of researchers have carried out studies about the relationship between aerosol characteristics and its driving factors. Yu et al. [7] investigated aerosol optical properties in Beijing with AERONET measurements between 2002 and 2007, finding an obvious seasonal variation with higher AOD values in spring and summer. Kang

[*] Email: vdtuyen@hunre.edu.vn

et al. [8] conducted research about aerosol optical property in Nanjing through ground-based measurements from September 2007 to August 2008, and arrived at the conclusion that aerosol over Nanjing mainly contained the mixed type, urban-industrial type, and biomass burning type. Che et al. [9] carried out a research on aerosol pollution in eastern China with ground-based measurements between 2011 and 2015 from seven observation sites, pointing out that-different from northern China - AOD in the Yangtze River Delta in July and August is lower than in January and February because of particle dispersion. Qin et al. [10] analyzed 38 years (1980-2017) of spatial and temporal variations of AOD in China using AOD records derived from MODIS atmosphere products and the MERRA-2 dataset. The results showed that dust aerosol (25.43%) and SO_4AOD (49.51%) were found to be the main driving factors for the spatial and temporal variations of AOD values. The GDP, population density, and passenger traffic volume were found to be the main socioeconomic drivers for AOD distributions. Relatively larger AOD values were mainly found in urban land and land covered by water, while lower AOD values were found in grassland and permanent glacier areas [10]. Most recently, Sun et al. (2020) studied spatial and temporal variation of AOD and optical depth of different aerosol types derived from the second Modern-Era Retrospective analysis for Research and Applications (MERRA-2) over the South China Sea (SCS) between 1980 and 2020 [11]. It was found that the correlation coefficient between total AOD and SO_4AOD from 1980 to 2020 was about 0.93, indicating SO_4AOD was the driving factor of TAOD variation [11]. When analyzing the spatial and temporal variations of AOD values over mainland China during 1973-2014 using the KM-Elterman method, Zhang et al. [12] showed that the estimated AOD values were in good agreement with AOD values derived from MODIS products ($R = 0.942$). It was also found that the North China Plain, Yangtze River Delta, Central China, Sichuan Basin, and Pearl River Delta were the areas with trends of rapidly increasing trend of AOD values; Southwest China was found to be an area with a significant decreasing trend of AOD values [12].

In recent years, air quality in northern Vietnam, especially in the area of Hanoi city, is strongly impacted by the northeast monsoon cycles that create periodic changes in the air mass pathways and the meteorological conditions [13]. Therefore, Hanoi, Vietnam’s capital, has suffered bouts of repeated and continuous air pollution with high ambient levels of particulate matter in the last decades [13]. When using Landsat 8 OLI satellite images to estimate PM 10, Hung et al. [14, 15] have also indicated that PM10 concentration is relatively high in urban areas of Hanoi city. Most recently, IQAir ranked Hanoi 12 out of 62 cities in a list of the world’s most polluted capital regions [16].

However, few studies have been made for analyzing the relationship of driving factors of AOD values in different land use and land cover over Hanoi city. Therefore, this study aims to investigate the relationship of land use and land cover and AOD variation using remotely sensed images acquired in winter in Hanoi city.

2. Materials and methodology

2.1. Materials

In this study, Landsat 9 Collection 2 Level 2 Science Product (L2SP) images with a spatial resolution of 30 m acquired on November 2, 2022 (Figure 1) and AOD at a spatial resolution of 1 km derived from MODIS MCD19A2 products were used in the study. The Landsat 9 images were downloaded from the United States Geological Survey (USGS – https://earthexplorer.usgs.gov/) website. Whereas, MODIS MCD19A2 products were downloaded from the Worldview tool (https://worldview.earthdata.nasa.gov).

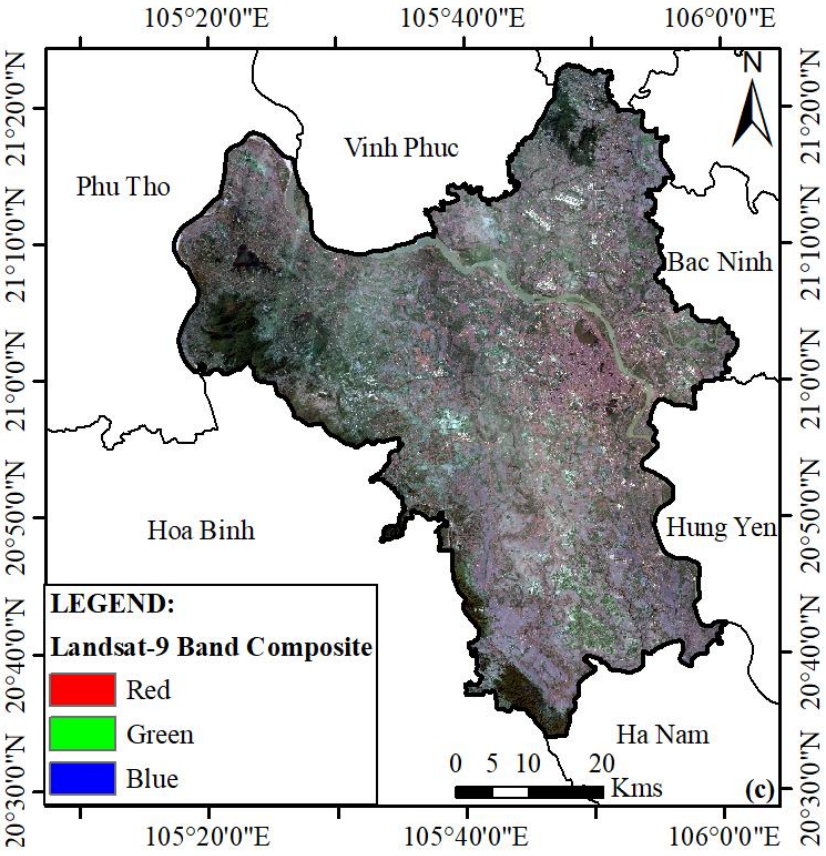

Figure 1. Landsat 9 true color composite in Hanoi city.

Landsat 9, launched on September 27, 2021 at 1:12PM CST from Vandenberg Air Force Base, California, onboard a United Launch Alliance Atlas V 401 rocket. Landsat 9 carries the Operational Land Imager 2 (OLI-2), built by Ball Aerospace &

Technologies Corporation, Boulder, Colorado, and the Thermal Infrared Sensor 2 (TIRS-2), built at the NASA Goddard Space Flight Center, Greenbelt, Maryland. Northrop Grumman designed and fabricated the spacecraft and integrated the two instruments. The satellite carries two science instruments, the OLI-2 and the TIRS-2. The OLI-2 captures observations of the Earth's surface in visible, near-infrared, and shortwave-infrared bands, and TIRS-2 measures thermal infrared radiation, or heat, emitted from the Earth's surface as shown in Table 1.

Table 1. Landsat 9 spectral bands

Band	Name	Wavelength (μm)	Spatial resolution (m)
1	Visible Coastal Aerosol	0.43 - 0.45	30
2	Visible Blue	0.45 - 0.51	30
3	Visible Green	0.53 - 0.59	30
4	Red	0.64 - 0.67	30
5	Near-Infrared	0.85 - 0.88	30
6	Sortware infrared	1.57 - 1.65	30
7	Sortware infrared	2.11 - 2.29	30
8	Panchromatic (PAN)	0.50 - 0.68	15
9	Cirrus	1.36 - 1.38	30
10	Thermal infrared	10.60 - 11.19	100
11	Thermal infrared	11.50 - 12.51	100

2.2. Methodology

2.2.1. Maximum likelihood classification

Maximum likelihood classification (MLC) was executed following a specific protocol of our steps: (i) the training samples for each of the LULC classes were selected from the color combination image by on-screen digitization of polygons of representative sites; (ii) the pixels with similar spectral signatures enclosed within these polygons were grouped together into one land cover class and saved; (iii) once the spectral signature was deemed satisfactory, the spectral signature was input into the MLC without prior probability; and (iv) thematic raster layers were generated representing LULC in the study area. It is worthwhile to mention that a spectral signature is satisfactory when confusion in clustering of pixels among the land covers to be mapped is minimal [17, 18].

In this study, classification accuracy was empirically identified using randomly selected reference sample points which were compared against the classified images. The percentage of the correctly/erroneously labeled pixels from each class in the image

was estimated. This comparison produced error matrices which represent the base of the accuracy assessment process and provides detailed information of the agreement between the classification results and reference information [19]. For each image, overall accuracy, producer's accuracy, user's accuracy, and Kappa coefficient were calculated. The overall accuracy and Kappa coefficient were determined using equations (1) and (2):

$$\text{Overall accuracy} = \frac{\sum_{i=1}^{r} x_{ii}}{x}, \quad (1)$$

where x_{ii} is the diagonal elements in the error matrix, x is the total number of samples in error matrix.

$$K = \frac{N \cdot \sum_{i=1}^{r} x_{ii} - \sum_{i=1}^{r} (x_{i+} * x_{+i})}{N^2 - \sum_{i=1}^{r} (x_{i+} * x_{+i})}, \quad (2)$$

where *k is* Kappa coefficient*; r* is the number of rows in the error matrix; x_{ii} is the number of observations in row *i* and column *i*; x_{i+} and x_{+i} are the marginal totals of row *i* and column *i* respectively; and *N* is the total number of observations (pixels) [20]. Kappa value of 1 indicates perfect agreement and values less than 1 imply less than perfect agreement. Values lower than 0.4 represent poor agreement, values from 0.4 to 0.55 represent fair agreement, values from 0.55 to 0.7 represent good agreement, values from 0.7 to 0.85 represent very good agreement, and values higher than 0.85 represent excellent agreement [21].

In a confusion matrix, the class-specific producer's accuracy and user's accuracy, and overall accuracy are presented and used to evaluate the LULC classification results. Among these three types of classification accuracy, the producer's accuracy of a given class is calculated solely on the basis of training pixels of that class. The number of training pixels in other classes and their classification do not affect the producer's accuracy of a given class. By contrast, calculations of the class-specific user's accuracy and overall accuracy involve the number of training pixels that are assigned to all individual classes. Consequently, changing the proportions of the training pixels of individual LULC classes affects the user's accuracy and the overall accuracy.

2.2.2. Assessment of the relationship between land use/land cover and AOD variation

Once, the LULC types were extracted from Landsat 9 remotely sensed images, the AOD variation for each LULC type acquired from MODIS imagery was then extracted using the mask method. The statistical parameters (minimum, the 5^{th}, mean, the 95^{th}, maximum and standard deviation) for the AOD variation in each LULC were summarized and compared.

3. Result and discusion

3.1. Analysis of land use and land cover

In this study, a total of 105 random points were generated in ArcGIS software and converted random points to KML in order to verify them from Google Earth for accuracy assessment. Google Earth software was used to measure of how many ground truth pixels are correctly classified. The confusion matrix was shown in Table 2. It can be seen from this table the overall accuracy and Kappa coefficient of LULC classification was estimated as 88.79% and 0.86, respectively. Specifically, the pecentage of 100, 95, 100, 78.95, 82.61 and 85.71 of the training pixels of the classes water bodies, built-up land, forest, greening land, crop land and river sand were correctly classified, respectively. These resulted in 90.91, 79.17, 88.89, 90.48, 95.83, 85.71% user's accuracy for water bodies, built-up land, forest, greening land, crop land and river sand were correctly classified, respectively. The lowest user's accuracy of 79.17% is for the built-up land class because a higher number of pixels from the greening land and crop land class would be misclassified into the built-up class.

Table 2. Confusion matrix for LULC types

LULC	Water bodies	Built-up land	Forest	Greening land	Crop land	River sand	User's accuracy
Water bodies	20	0	0	0	2	0	90.91
Built-up land	0	19	0	3	2	0	79.17
Forest	0	0	16	1	0	1	88.89
Greening land	0	0	2	19	0	0	90.48
Crop land	0	1	0	0	23	0	95.83
River sand	0	1	0	0	0	6	85.71
Producer's accuracy	100.00	90.48	88.89	82.61	100.00	85.71	
Overall accuracy = 88.79; Kappa coefficient = 0.86							

The distribution of land use, land cover in Hanoi city and its corresponding areas were shown in Figure 2 and statistically summarised in Table 3, respectively. Data from

Table 3 illustrates the built-up land class was ranked the largest with an area 161894.6 ha accounting for approximately 48.3% of the total study area. Built-up land was mainly distributed in 12 urban districts and a district-leveled town (or simply town) in the city centre (Figure 2). Whereas, the greening land and crop land class was ranked the second and the third largest with their corresponding areas of 68817.5 ha (20.5%) and 55824.2 ha (16.6%). These two classes were mainly concentrated in 17 rural districts in the south, north and west of Hanoi metropolitan area. It was then followed by the water bodies, forest and river sand classes with areas of 29869.4 ha (8.9%), 18611.3 ha (5.5%), and 341.1 ha (0.1%), respectively.

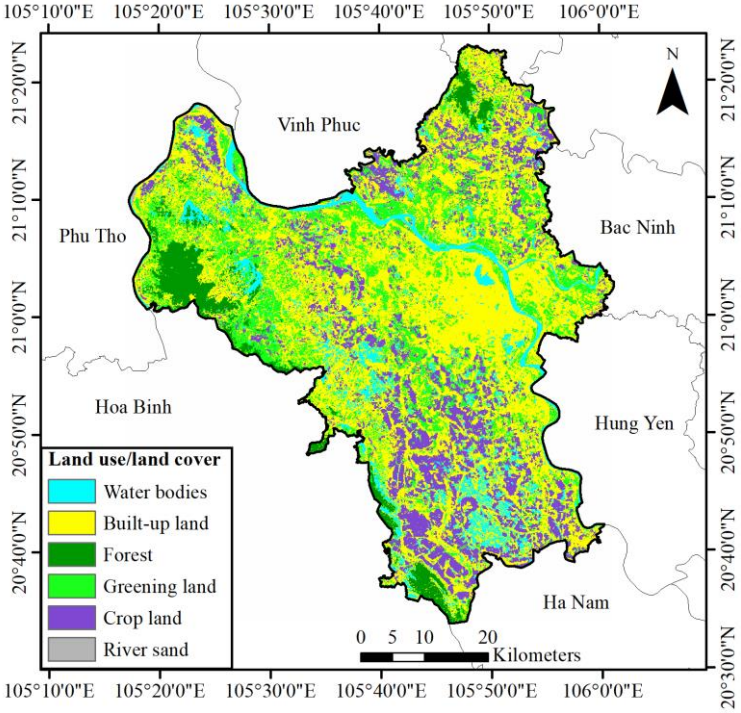

Figure 2. Map of land use and land cover.

Table 3. Areas of land use and land cover

Land use/ Land cover	**Area (ha)**	**Percentage (%)**	**Cumulative percentage (%)**
Water bodies	29869.4	8.9	8.9
Built-up land	161894.6	48.3	57.2
Forest	18611.3	5.5	62.7
Greening land	68817.5	20.5	83.3
Crop land	55824.2	16.6	99.9
River sand	341.1	0.1	100.0
Total	**335358.1**	**100.0**	**100.0**

3.2. Analysis of the relationship between land use/land cover and AOD variation

In this study, the AOD values ranged from 0.02 to 0.48 which were obtained from MODIS imagery acquired on November 1, 2022. What can be seen from the spatial distribution of AOD as shown in Figure 3 is that AOD values were relatively high in the central and southwestern areas of Hanoi city and low in mountainous areas with sparse vegetation in the north and west of Hanoi. Particularly, high and very high AOD values of above 0.4 appeared in the south of the study area.

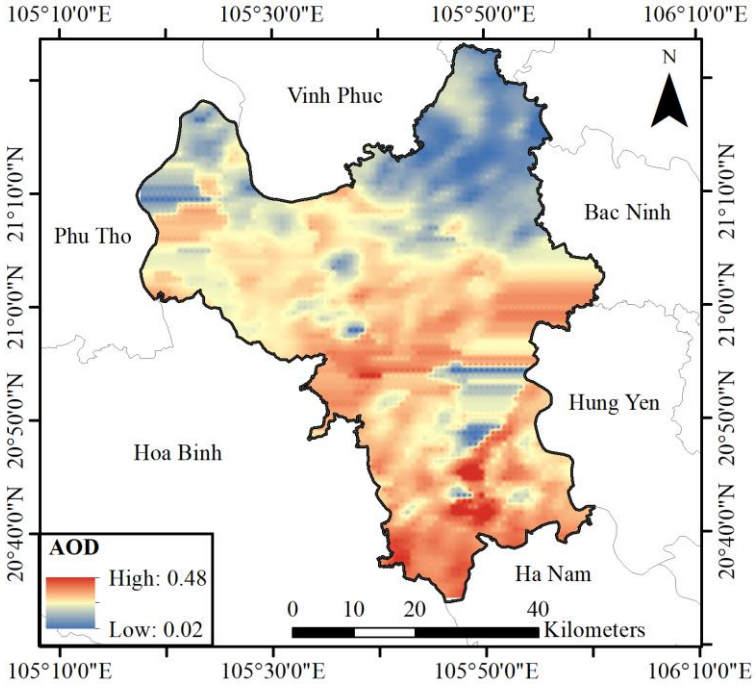

Figure 3. Map of AOD.

Table 4. Descriptive statistics of AOD for each LULC type

LULC	AOD					
	Min	**Min (5^{th})**	**Mean**	**Max (95^{th})**	**Max**	**SDEV**
Water bodies	0.0	0.09	0.26	0.38	0.48	0.07
Built-up land	0.0	0.12	0.24	0.33	0.48	0.07
Forest	0.0	0.17	0.19	0.33	0.40	0.05
Greening land	0.0	0.09	0.23	0.32	0.47	0.06
Crop land	0.0	0.13	0.23	0.34	0.46	0.08
River sand	0.0	0.14	0.19	0.22	0.30	0.03

Notes: *Min, Mean, Max, SDEV are the minimum, mean and maximum values; Min (5^{th}) and Max (95^{th}) are the 5^{th} and 95^{th} percentile of AOD which are the lowest and highest values left when the bottom 95% and top 5% of a numerically sorted set of collected data is discarded, respectively.*

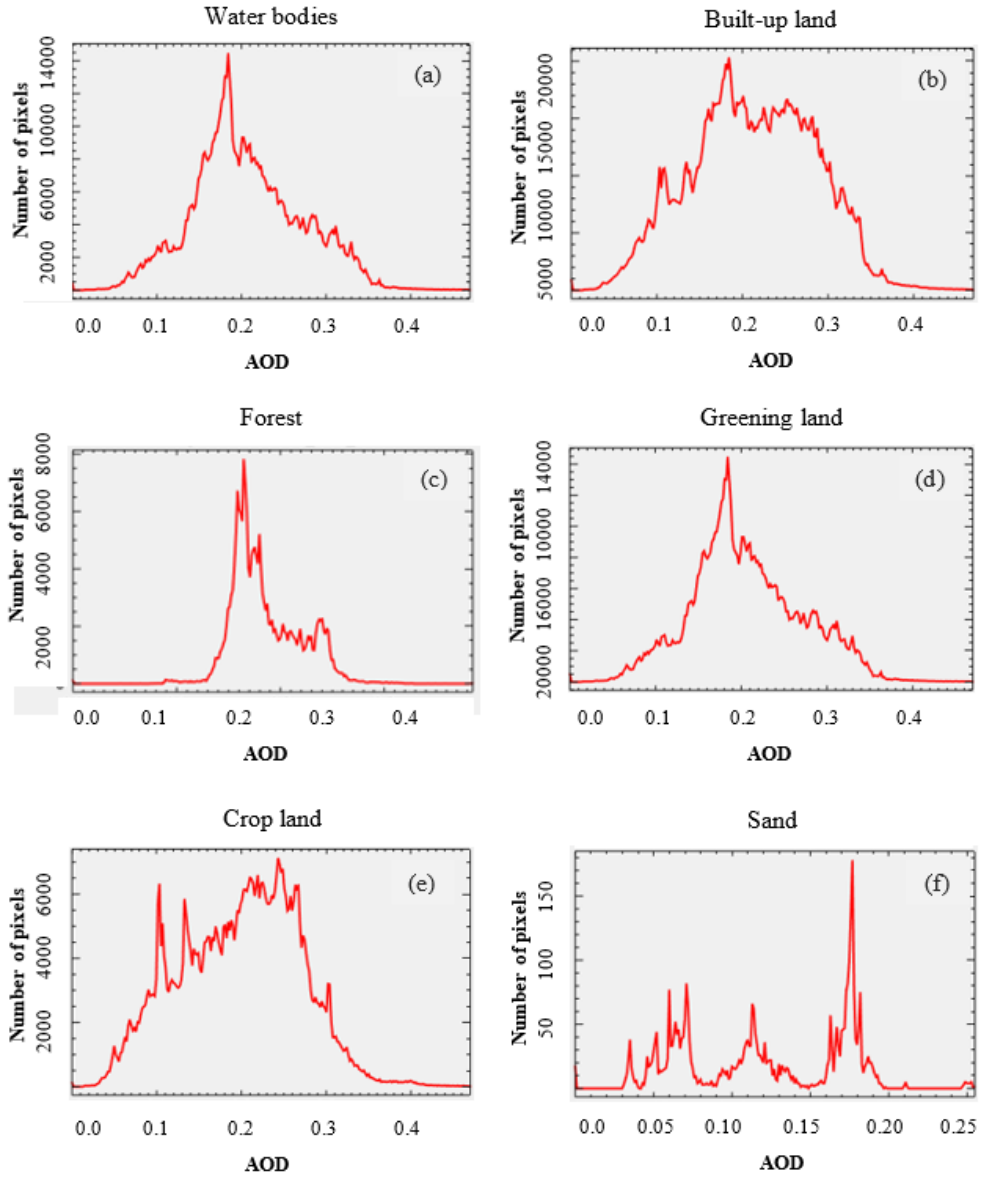

Figure 4. Histograms of AOD variation with different types of land use and land cover.

The AOD variation of each corresponding LULC type was shown in Figure 4 and statistically summarised in Table 4, respectively. As can be seen from Table 4, the minimum value of AOD for each LULC type is almost zero, however, the min values at the 5^{th} percentile were different for each LULC type. Specifically, forest, river sand, and crop land appeared to have the largest values with 0.17, 0.14 and 0.13, respectively. It is followed by built-up land, water bodies and greening land with values of 0.12 and 0.09, respectively. The largest mean AOD value belongs to water cover (0.26), followed by built-up land (0.24), greening land and crop land (0.23) and forest and sand (0.19),

respectively. Data from Table 4 also illustrates that, the maximum AOD values of each LULC type exceeded 0.4, of which the largest values were found for classes water bodies and built-up land (0.48), then greening land (0.47), crop land (0.46), forest (0.4), and sand (0.30), respectively. This result indicates that high AOD value tends to be concentrated in areas of water surface and built-up land. Low SDEV means data are clustered around the mean, and high SDEV indicates data are more spread out. It can be seen from Figure 4 and Table 4 that AOD value of crop land, water bodies and built-up land tends to spread out with the corresponding values of 0.08 and 0.07, respectively. Whereas, the AOD value of river sand, forest and greening land tends to be clustered. These results show that there was a close relationship between the AOD variation and water bodies and built-up land. This relationship could be a positive correlation between these two types of LULC. This is quite consistent with the fact that one of the main sources of high AOD values is from the residential and industrial areas. Meanwhile, lower AOD values were usually distributed in greening land and crop land. The lowest AOD values were mainly concentrated in such LULC as forest and river sand. This is inline with the fact that these are not sources of high AOD values.

4. Conclusion

This study aims to assess the relationship between AOD variation and different LULC types. LULC types were first classified from Landsat 9 remotely sensed images using maximum likelihood classification method. The AOD variation for each LULC type was then extracted using the mask method. The statistical parameters for the AOD variation in each LULC were summarized and compared. A case study of Hanoi city has shown that there existed a close relationship (a positive correlation) between the AOD variation and water bodies and built-up land. Lower AOD values were usually distributed in greening land and crop land. Whereas, the lowest AOD values were mainly concentrated in forest and river sand. These findings have significant implications for the more fundamental understanding of the impacts of different LULC types on the AOD variation.

Acknowledgements

This study was financially supported and funded by the 562 ministry-level basic science program in chemistry, life science, earth science and sea science for 2017-2025 (Grant number: TNMT.2023.562.07).

References

[1] Bellouin, N.; Boucher, O.; Haywood, J.; Reddy, M. S., "Global estimate of aerosol direct radiative forcing from satellite measurements," *Nature*, 438, 1138-1141, 2005. DOI: 10.1038/nature04348

[2] Kirkevag, A.; Iversen, T., "Global direct radiative forcing by process-parameterized aerosol optical properties," *J. Geophys. Res. Atmos.*, 107, 2002. DOI: 10.1029/2001JD000886

[3] Filip, L.; Stefan, S., "Study of the correlation between the near-ground PM10 mass concentration and the aerosol optical depth," *J. Atmos. Sol. Terr. Phys.*, 73, 1883-1889, 2011. DOI: 10.1016/j.jastp.2011.04.027

[4] Charlson, R. J.; Schwartz, S. E.; Hales, J. M.; Cess, R. D.; Coakley, J. A.; Hansen, J. E.; Hofmann, D. J., "Climate forcing by anthropogenic aerosols," *Science*, 255, 423-430, 1992. DOI: 10.1126/science.255.5043.423

[5] Sun, E., Fu, C., Yu, W., Xie, Y., Lu, Y., & Lu, C., "Variation and Driving Factor of Aerosol Optical Depth over the South China Sea from 1980 to 2020," *Atmosphere*, 13(3), 372, 2022. DOI: 10.3390/atmos13030372

[6] Zhao, B.; Jiang, J.; Diner, D.; Su, H.; Gu, Y.; Liou, K.; Jiang, Z.; Huang, L.; Takano, Y.; Fan, X.; et al., "Intra-annual variations of regional aerosol optical depth, vertical distribution, and particle types from multiple satellite and ground-based observational datasets," *Atmos. Chem. Phys.*, 18, 11247-11260, 2018. DOI: 10.5194/acp-18-11247-2018

[7] Yu, X.; Zhu, B.; Zhang, M., "Seasonal variability of aerosol optical properties over Beijing," *Atmos. Environ.*, 43(26), 4095-4101, 2009. DOI: 10.1016/j.atmosenv.2009.03.061

[8] Kang, N.; Kumar, K.; Yu, X.; Yin, Y., "Column-integrated aerosol optical properties and direct radiative forcing over the urban industrial megacity Nanjing in the Yangtze River Delta, China," *Environ. Sci. Pollut. Res.*, 23, 17532-17552, 2016. DOI: 10.1007/s11356-016-6953-1

[9] Che, H.; Qi, B.; Zhao, H.; Xia, X.; Eck, T.F.; Goloub, P.; Dubovik, O.; Estelles, V.; Cuevas-Agulló, E.; Blarel, L.; et al., "Aerosol optical properties and direct radiative forcing based on measurements from the China Aerosol Remote Sensing Network (CARSNET) in eastern China," *Atmos. Chem. Phys.*, 18, 405-425, 2018. DOI: 10.5194/acp-18-405-2018

[10] Qin, W., Liu, Y., Wang, L., Lin, A., Xia, X., Che, H.,... & Zhang, M., "Characteristic and driving factors of aerosol optical depth over mainland China during 1980-2017," *Remote Sensing*, 10(7), 1064, 2018. DOI: 10.3390/rs10071064

[11] Sun, E., Fu, C., Yu, W., Xie, Y., Lu, Y., & Lu, C., "Variation and Driving Factor of Aerosol Optical Depth over the South China Sea from 1980 to 2020," *Atmosphere*, 13(3), 372, 2022. DOI: 10.3390/atmos13030372

[12] Zhang, Z. Y.; Wu, W. L.; Wei, J.; Song, Y.; Yan, X. T.; Zhu, L. D.; Wang, Q., "Aerosol optical depth retrieval from visibility in China during 1973-2014," *Atmos. Environ.*, 171, 38-48, 2017. DOI: 10.1016/j.atmosenv.2017.09.004

[13] Phung-Ngoc, B. A., Dieudonné, E., Delbarre, H., Deboudt, K., Nguyen, S. T., Bui, V. H.,... & Nguyen-Thi, H. T. "Intricate behavior of winter pollution in Hanoi over the 2006-2020 semi-climatic period," *Atmospheric Environment*, 300, 119669, 2023. DOI: 10.1016/j.atmosenv. 2017.09.004

[14] Hung, N. N., Anh, T. V., Vinh, P. Q., Binh, N. T., & Hoang, V. V., "Model to determine PM10 dust in the air in Hanoi area using Landsat 8 OLI satellite image data and visual dust measurement data," *VNU Science Journal: Earth and Environmental Sciences*, 1, 23-36, 2018. DOI: 10.25073/2588-1094/vnuees.4146

[15] Hung, N. N., Hang, L. M., Anh, T. V., & Hai, L. V. H. "Assessment the effect of atmospheric correction algorithms for monitoring PM10 concentration by using Landsat 8OLI data: A case study in Hanoi, Vietnam," *Russian Journal of Earth Sciences*, 20(5), ES5002-ES5002, 2020. DOI: 10.2205/2020ES000701

[16] QAir. World Air Quality Report. IQAir: Godard Hector, Switzerland, 2019.

[17] Geo, J., & Liu, Y., "Determination of land degradation causes in Tongyu county Northeast China via land cover change detection," *International Journal of Applied Earth Observation Geoinformation*, 12 (1), 9-16, 2010. DOI: 10.1016/j.jag.2009.08.003

[18] Butt, A., Shabbir, R., Ahmad, S.S., & Aziz, N., "Land use change mapping and analysis using remote sensing and GIS: A case study of Simly Watershed, Islamabad, Pakistan," *Egyptian Journal of Remote Sensing and Space Science*, 18(2), 251-259, 2015. DOI: 10.1016/j.ejrs.2015.07.003

[19] Congalton, R. G., & Green, K., *Assessing the accuracy of remotely sensed data: Principles and practices*, CRC Press, 2009.

[20] Jensen, J. R., *Introductory digital image processing: A remote sensing perspective*, 3rd ed, Clarke, K. C., Ed., Prentice Hall, Upper Saddle River, New Jersey, USA, 2005.

[21] Monserud, R. A., & Leemans, R., "Comparing global vegetation maps with the Kappa statistic," *Ecological Modelling*, 62(4), 275-293, 1992. DOI: 10.1016/0304-3800(92)90003-W

ĐÁNH GIÁ MỐI QUAN HỆ GIỮA SỰ BIẾN THIÊN CỦA ĐỘ DÀY QUANG HỌC SOL KHÍ VỚI LỚP PHỦ MẶT ĐẤT/SỬ DỤNG ĐẤT KHU VỰC THÀNH PHỐ HÀ NỘI

Vũ Danh Tuyên[a], Hoàng Anh Huy[a], Nguyễn Tiến Thành[a]

[a]*Trường Đại học Tài nguyên và Môi trường Hà Nội*

Tóm tắt: *Nghiên cứu này đánh giá mối quan hệ giữa AOD được thu nhận từ bộ cảm MODIS và các loại hình lớp phủ mặt đất/sử dụng đất (LULC). Các loại hình LULC được phân loại từ ảnh Landsat 9 bằng thuật toán xác suất cực đại (MLC). Sự biến thiên của AOD cho từng loại LULC sau đó được trích xuất bằng phương pháp mặt nạ. Các tham số thống kê cho sự biến thiên của AOD đối với mỗi loại hình LULC được tính toán và so sánh với nhau. Kết quả nghiên cứu đã chỉ ra có mối quan hệ chặt chẽ (tương quan thuận) giữa sự thay đổi AOD với nước mặt và đất xây dựng. AOD thấp hơn thường phân bố trên lớp đất phủ xanh và lớp đất trồng trọt. Trong khi đó, giá trị AOD thấp nhất chủ yếu tập trung tại rừng và cát sông.*

Từ khóa: Mối quan hệ; lớp phủ/sử dụng đất; độ dày quang học sol khí; ảnh vệ tinh viễn thám Landsat 9 và MODIS.

Received: 09/04/2023; *Revised:* 08/06/2023; *Accepted:* 23/06/2023; *Published:* 30/06/2023

❑